Hyperspectral remote sensing for shallow waters: 2. Deriving bottom depths and water properties by optimization

Zhongping Lee, Kendall L. Carder, Curtis D. Mobley, Robert G. Steward, and Jennifer S. Patch

In earlier studies of passive remote sensing of shallow-water bathymetry, bottom depths were usually derived by empirical regression. This approach provides rapid data processing, but it requires knowledge of a few true depths for the regression parameters to be determined, and it cannot reveal in-water constituents. In this study a newly developed hyperspectral, remote-sensing reflectance model for shallow water is applied to data from computer simulations and field measurements. In the process, a remote-sensing reflectance spectrum is modeled by a set of values of absorption, backscattering, bottom albedo, and bottom depth; then it is compared with the spectrum from measurements. The difference between the two spectral curves is minimized by adjusting the model values in a predictor–corrector scheme. No information in addition to the measured reflectance is required. When the difference reaches a minimum, or the set of variables is optimized, absorption coefficients and bottom depths along with other properties are derived simultaneously. For computer-simulated data at a wind speed of 5 m/s the retrieval error was 5.3% for depths ranging from 2.0 to 20.0 m and 7.0% for total absorption coefficients at 440 nm ranging from 0.04 to 0.24 m^{-1}. At a wind speed of 10 m/s the errors were 5.1% for depth and 6.3% for total absorption at 440 nm. For field data with depths ranging from 0.8 to 25.0 m the difference was 10.9% ($R^2 = 0.96$, $N = 37$) between inversion-derived and field-measured depth values and just 8.1% ($N = 33$) for depths greater than 2.0 m. These results suggest that the model and the method used in this study, which do not require *in situ* calibration measurements, perform very well in retrieving in-water optical properties and bottom depths from above-surface hyperspectral measurements.

OCIS codes: 010.4450, 280.0280.

1. Introduction

The signals measured by a sensor from above the water surface of a shallow site contain surface-reflected skylight, radiance reflected from the bottom, and path radiance from the water column. For the bottom depth to be retrieved, the surface-reflected light and the water-column contributions have to be removed, and the optical properties of the water column have to be known or derived. In earlier studies[1–8] values for water-column contributions were usually derived from adjacent deep waters[1,2,4,9] and light attenuation properties were assumed to be known *a priori*[1] or empirically derived from an image by regression[4,7] by using a few true depths provided by lidar[9] or on-site ship measurements.

However, the above-preferred conditions rarely exist. First, path radiance from deep waters is not the same as that from the water column of shallow waters, even if the optical properties are the same.[8–12] Second, for estuarine or coastal waters, the color constituents of the water can be patchy, so the optical properties throughout an image may not always be the same. Third, known depths are not always available for deriving the regression parameters. And finally, owing to land runoff and tidal influences, coastal water properties change rapidly. A known optical value from a different time may not be the same as when a remote sensor takes measurements. To overcome these obstacles, it is desirable to derive simultaneously bottom depths and albedo and the optical properties of the water column.

In this study a newly developed semianalytical, remote-sensing reflectance R_{rs} (see Table 1 for sym-

Z. Lee, K. L. Carder, R. G. Steward, and J. S. Patch are with the Department of Marine Science, University of South Florida, St. Petersburg, Florida 33701. The e-mail address for Z. Lee is zplee@monty.marine.usf.edu. C. D. Mobley is with Sequoia Scientific, Incorporated, 9725 S.E. 36th Street, Suite 308, Mercer Island, Washington 98040.

Received 11 September 1998; revised manuscript received 11 March 1999.

0003-6935/99/183831-13$15.00/0

Table 1. Symbols

Symbols	Description	Units
a_w	Absorption coefficient of pure water	m^{-1}
a_ϕ	Absorption coefficient of phytoplankton pigments	m^{-1}
a_g	Absorption coefficient of gelbstoff	m^{-1}
a	Absorption coefficients of the total ($= a_w + a_\phi + a_g$)	m^{-1}
b_b	Backscattering coefficients	m^{-1}
b_p	Scattering coefficients of suspended particles	m^{-1}
b_{bp}	Backscattering coefficients of suspended particles	m^{-1}
D	Distribution function	
E_d	Downwelling irradiance	$W/nm/m^2$
$F(\theta)$	Surface Fresnel reflectance for angle θ	
H	Bottom depth	m
L_u	Above-surface upwelling radiance	$W/m^2/nm/sr$
L_w	Water-leaving radiance	$W/m^2/nm/sr$
r_{rs}	Subsurface remote-sensing reflectance	sr^{-1}
$r_{rs}{}^B$	Subsurface remote-sensing reflectance from bottom reflection	sr^{-1}
$r_{rs}{}^C$	Subsurface remote-sensing reflectance from water-column scattering	sr^{-1}
R_{rs}	Above-surface remote-sensing reflectance	sr^{-1}
T_{rs}	Total remote-sensing reflectance ($= L_u/E_d$)	sr^{-1}
S_{rs}	Sky input ($= L_{sky}/E_d$)	sr^{-1}
[chl-a]	Chlorophyll-a concentration	mg/m^3
κ	Attenuation coefficient ($= a + b_b$)	m^{-1}
ρ	Bottom albedo	
θ_w	Subsurface solar zenith angle	rad

bols used in this text) model (SA-model) for shallow water[13] was applied to both computer-simulated and field-measured data. In the model, downward and upward diffuse attenuation coefficients are explicitly described as functions of the absorption and backscattering coefficients as are the water-column contributions. In the derivation process a remote-sensing reflectance spectrum is simulated with the SA-model by introducing a set of coefficients for absorption a, backscattering b_b, bottom albedo ρ, and bottom depth H. Then one determines a difference measure by comparing the model and the measurement spectra. Using a computer program, one repeats this predictor–corrector process by adjusting the values of a, b_b, H, and ρ until the difference measure reaches a minimum and the values of a, b_b, H, and ρ are derived. Only then are the derived values compared with measured values. In the derivation only the spectral shape of the bottom albedo was assumed known. The albedo intensity, however, was allowed to change from place to place. No information in addition to the $R_{rs}(\lambda)$ from measurements is required in the derivation process. From the derived absorption coefficients, concentrations of in-water chlorophyll-a or gelbstoff, for example, can be derived.[14]

2. Modeling of Remote-Sensing Reflectance R_{rs}

Remote-sensing reflectance R_{rs} is defined as the ratio of the water-leaving radiance to downwelling irradiance just above the surface. R_{rs} is an apparent optical property[15] controlled by the absorption and the scattering properties of the constituents in the water, the bottom albedo and the bottom depth, is influenced by fluorescence and Raman emission,[16] and is modestly affected by the angles of solar input and output radiance.[17] In general, for optically shallow waters with vertical homogeneity, and when the inelastic scattering contributions are ignored,

$$R_{rs}(\lambda) = f[a(\lambda), \beta(\lambda), \rho(\lambda), H, \theta_w, \theta, \varphi], \qquad (1)$$

where $a(\lambda)$ is the absorption coefficient, $\beta(\lambda)$ is the volume scattering function, $\rho(\lambda)$ is the bottom albedo, H is the bottom depth, θ_w is the subsurface solar zenith angle, θ is the subsurface viewing angle from nadir, and φ is the viewing azimuth angle from the solar plane. For brevity, wavelength dependence may not be explicitly included unless required for clarity.

Recently, by use of Hydrolight 3.0,[18] an SA model for nadir-viewing R_{rs} was developed[13] (a concise overview is in Appendix A):

$$R_{rs} \approx \frac{0.5 r_{rs}}{1 - 1.5 r_{rs}}, \qquad (2)$$

where r_{rs} (the subsurface remote-sensing reflectance or the ratio of the upwelling radiance to the downwelling irradiance evaluated just below the surface) is

$$\begin{aligned} r_{rs} &= r_{rs}{}^C + r_{rs}{}^B \\ &\approx r_{rs}{}^{dp}\left(1 - \exp\left\{-\left[\frac{1}{\cos(\theta_w)} + D_u{}^C\right]\kappa H\right\}\right) \\ &\quad + \frac{1}{\pi}\rho \exp\left\{-\left[\frac{1}{\cos(\theta_w)} + D_u{}^B\right]\kappa H\right\}, \end{aligned} \qquad (3)$$

and r_{rs}^{dp} (remote-sensing reflectance for optically deep water) is

$$r_{rs}^{dp} \approx (0.084 + 0.170u)u. \tag{4}$$

The optical path-elongation factors for scattered photons from the water column D_u^C and bottom D_u^B are

$$D_u^C \approx 1.03(1 + 2.4u)^{0.5}, \qquad D_u^B \approx 1.04(1 + 5.4u)^{0.5} \tag{5}$$

with

$$u = b_b/(a + b_b), \qquad \kappa = a + b_b, \tag{6}$$

where[19,20]

$$b_b = b_{bw} + b_{bp} \tag{7}$$

$$a = a_w + a_\phi + a_g. \tag{8}$$

Note that both u and κ in Eqs. (6) are inherent optical properties,[15] and the combination of Eqs. (2)–(6) provides the expression for R_{rs}. In Eq. (2) $0.5/(1 - 1.5r_{rs})$ is the water-to-air divergence factor and $(1 - 1.5r_{rs})$ accounts for the internal reflection of the water–air interface, which is important for very shallow and/or very turbid waters; b_{bw} is the backscattering coefficient of seawater, while b_{bp} is the backscattering coefficient of particles.

These equations describe the model for nadir-viewing sensors. However, remote sensors view the target at a series of angles, not just at nadir. For the above equations to be used for other viewing angles, model adjustments are necessary. It has been found, however, that even for case 1 waters[21] there is no simple analytical function that can accurately model r_{rs} for different viewing angles,[17] especially when the situation is complicated by shallow and turbid waters, where more multiple scattering occurs.

By fitting Hydrolight-generated r_{rs} values for different viewing angles with empirical functionality, we found that Eqs. (2)–(6) are still generally applicable if we make a slight adjustment:

$$r_{rs} \approx r_{rs}^{dp}\left(1 - \exp\left\{-\left[\frac{1}{\cos(\theta_w)} + \frac{D_u^C}{\cos(\theta)}\right]\kappa H\right\}\right) + \frac{1}{\pi}\rho \exp\left\{-\left[\frac{1}{\cos(\theta_w)} + \frac{D_u^B}{\cos(\theta)}\right]\kappa H\right\}, \tag{9}$$

with b_b of Eq. (7) adjusted to

$$b_b'(\lambda) = b_{bw}(\lambda) + \varepsilon(\lambda) b_{bp}(\lambda). \tag{10}$$

The term $1/\cos(\theta)$ in Eq. (9) accounts for the increased path length for larger viewing angles when the upwelling radiance field is not Lambertian; ε in Eq. (10) is an empirical parameter to account for the effects of changing view angles on the effective scattering, and it varies with angles of solar input and radiance output. For r_{rs} in the plane 90° to the solar plane, and to first order, ε can be approximated as

$$\varepsilon(\lambda) \approx 1.0 + [0.1 + 0.8 b_{bp}(\lambda)/b_b(\lambda)]\sin(\theta)\sin(\theta_w). \tag{11}$$

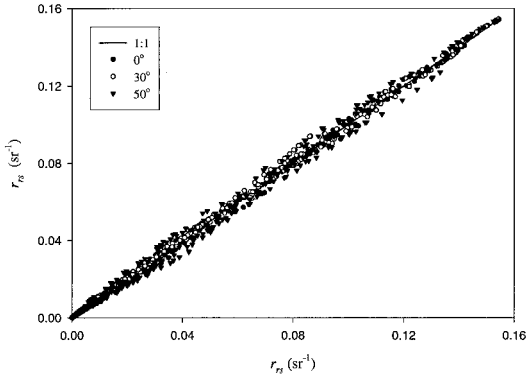

Fig. 1. Hydrolight-calculated r_{rs} (line) versus SA-model-determined r_{rs} (symbols) for three viewing angles.

Figure 1 presents r_{rs} data calculated with Hydrolight and the above SA-model for three viewing angles. This adjusted expression on average can explain Hydrolight-calculated r_{rs} values with an error of 6.1% for remote observations in the plane 90° to the solar plane. The maximum error was ~15% for cases with high turbidity and large viewing angles. Hence we limit our viewing angles to 30° from nadir at an azimuth of 90° from solar plane. For more accurate forward modeling at different viewing angles, numerical methods such as Hydrolight or Monte Carlo are needed. These methods, however, are slow and not appropriate for real-time applications. For the following inversion calculations the above model [approximation (9)] will be applied to computer-simulated and field-measured data, and the derived a and H values will be compared with actual values.

3. Inversion Method

A. General Description

A remote sensor located above the water surface measures the total upwelling radiance, not the remote-sensing reflectance. We thus derive the properties of the water body from the total remote-sensing reflectance T_{rs}, which is the ratio of the total upwelling radiance at some observation angle (θ_v, φ_v) to the downwelling irradiance above the surface. Above-surface downwelling irradiance can be easily measured or accurately calculated from existing models.[22]

T_{rs} and S_{rs} (sky input) are defined as[23]

$$T_{rs} = \frac{L_u}{E_d}, \qquad S_{rs} = \frac{L_{\text{sky}}}{E_d}. \tag{12}$$

T_{rs} includes R_{rs}, surface-reflected S_{rs}, and possible solar-glint effects. By correcting for the reflected skylight and solar glint, we can derive R_{rs} from T_{rs}. Traditionally, for nonturbid waters one performed this correction by subtracting a fraction (a value of surface Fresnel reflectance) of S_{rs} from T_{rs} and then by adjusting for sun glint by biasing the residual curve to 0 around 750 nm.[24] However, $R_{rs}(750)$ may not be zero for coastal waters and can vary from place

to place. This variance suggests that the value of $R_{rs}(750)$ for coastal waters may have to be derived.

It has been found that T_{rs} can be expressed as[23–25]

$$T_{rs}(\lambda) \approx R_{rs}(\lambda) + F(\theta)S_{rs}(\lambda) + \Delta, \tag{13}$$

where $F(\theta)$ is the surface Fresnel reflectance based on the viewing geometry and Δ is a spectrally constant offset.

If we define a quantity called raw-remote-sensing reflectance R_{rs}^{raw} as

$$R_{rs}^{\text{raw}}(\lambda) = T_{rs}(\lambda) - F(\theta)S_{rs}(\lambda), \tag{14}$$

approximation (13) can be rewritten as

$$R_{rs}^{\text{raw}}(\lambda) \approx R_{rs}(\lambda) + \Delta. \tag{15}$$

In approximation (15), $R_{rs}^{\text{raw}}(\lambda)$ is a known spectrum derived from above-surface measurements. If we replace $R_{rs}(\lambda)$ in approximation (15) by the expression of approximation (2), remote measurement of in-water optical properties is a process of spectrally decomposing approximation (15). Therefore the next important step is how to derive more accurately such environmental properties as absorption and bottom depth from approximation (15).

Each measured $R_{rs}^{\text{raw}}(\lambda)$ spectrum consists of at least three unknown spectra [$a(\lambda)$, $b_b(\lambda)$, and $\rho(\lambda)$] and two scalar unknowns (H and Δ). This composition suggests that, if the sensor has n channels, there are $(3n + 2)$ unknowns to be deduced. To solve for these many unknowns, additional relationships have to be established to reduce the number of unknowns (or increase the number of equations).

B. Parameterization

In Eq. (8) the values of $a_w(\lambda)$, the absorption coefficients of pure water, were taken from Pope and Fry.[26]

The absorption coefficient of phytoplankton pigments is $a_\phi(\lambda)$ which must be derived from remote measurements. We used a single-parameter model to simulate this spectrum[27]:

$$a_\phi(\lambda) = [a_0(\lambda) + a_1(\lambda)\ln(P)]P, \tag{16}$$

where $P = a_\phi(440)$ is the phytoplankton absorption coefficient at 440 nm. The empirical coefficients for $a_0(\lambda)$ and $a_1(\lambda)$ are presented in Ref. 13. This approach allows the $a_\phi(\lambda)$ curvature to change with $a_\phi(440)$, consistent with field observations, at least to first order.

The absorption coefficient of gelbstoff and detritus is $a_g(\lambda)$, which can be expressed as[20,28,29]

$$a_g(\lambda) = G\exp[-S(\lambda - 440)], \tag{17}$$

with $G = a_g(440)$. S is the spectral slope, and it has been reported in the range of 0.011–0.021 nm^{-1}.[20,30] Because G is a sum of gelbstoff and detritus absorption spectra, we used an S value of 0.015 nm^{-1} as a representative average in our inversion process.

Equation (10) is rewritten as

$$b_b'(\lambda) = b_{bw}(\lambda) + b_{bp}'(\lambda) \tag{18}$$

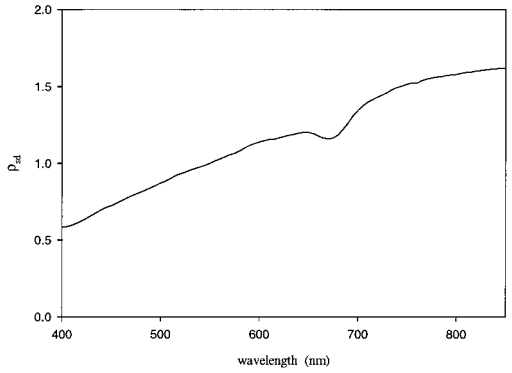

Fig. 2. A 550-nm normalized bottom-albedo spectrum.

with values for $b_{bw}(\lambda)$ taken from Morel.[31] We express $b_{bp}'(\lambda)$ as

$$b_{bp}' = X\left(\frac{400}{\lambda}\right)^Y, \tag{19}$$

where $X = b_{bp}'(400)$, which combines the particle-backscattering coefficient, viewing-angle information, as well as sea state into one variable. The spectral shape parameter Y is estimated by an empirical relationship[32]:

$$Y \approx 3.44[1 - 3.17\exp(-2.01\chi)], \tag{20}$$

with $\chi = R_{rs}^{\text{in}}(440)/R_{rs}^{\text{in}}(490)$. $R_{rs}^{\text{in}}(\lambda)$ is the initial estimate of $R_{rs}(\lambda)$ and is determined as follows:

$$R_{rs}^{\text{in}}(\lambda) = R_{rs}^{\text{raw}}(\lambda) - R_{rs}^{\text{raw}}(750). \tag{21}$$

We keep Y within the 0–2.5 range.

For $\rho(\lambda)$ a 550-nm-normalized, sand-albedo shape [$\rho_{sd}(\lambda)$] was used (Fig. 2). Note that only sandy environments were examined in the field tests. Therefore $\rho(\lambda)$ is expressed as

$$\rho(\lambda) = B\rho_{sd}(\lambda), \tag{22}$$

where B is the bottom albedo value at 550 nm.

With the above considerations there are six variables for Eq. (15): P, G, X, B, H, and Δ. These six variables uniquely influence the $R_{rs}^{\text{raw}}(\lambda)$ spectra, which avoids the possibility of a singularity arising from Eq. (15) unless the data are very noise. To overcome random noise and to always provide a measured value near the peak of the $R_{rs}(\lambda)$ curve, a hyperspectral data set was used. The six unknowns can be derived by minimizing the differences between R_{rs} curves that are modeled [approximation (2)] and measured as expressed by

$$\hat{R}_{rs}(\lambda) = R_{rs}^{\text{raw}}(\lambda) - \Delta. \tag{23}$$

An index for comparing the two R_{rs} curves was defined in Ref. 23,

$$err = \frac{\left[\sum_{400}^{675}(R_{rs} - \hat{R}_{rs})^2 + \sum_{750}^{830}(R_{rs} - \hat{R}_{rs})^2\right]^{0.5}}{\sum_{400}^{675}\hat{R}_{rs} + \sum_{750}^{830}\hat{R}_{rs}}, \tag{24}$$

Table 2. Input Values to Hydrolight Calculation Compared with Inversion-Derived Values

Input						Inversion					
[chl-a]	$a_\phi(440)$	$a_g(440)$	H	S	Y	$a_\phi(440)$	$a_g(440)$	H	S	Y	w
2.0	0.094	0.141	2.0	0.014	1.0	0.101	0.129	2.1	0.015	0.5	0.78
2.0	0.094	0.141	5.0	0.014	1.0	0.109	0.092	4.9	0.015	0.2	0.51
1.0	0.060	0.090	4.0	0.014	1.0	0.065	0.078	4.2	0.015	0.5	0.72
1.0	0.060	0.090	8.0	0.014	1.0	0.067	0.063	7.8	0.015	0.4	0.40
0.4	0.033	0.050	8.0	0.014	1.0	0.035	0.044	8.4	0.015	0.8	0.61
0.4	0.033	0.050	12.0	0.014	1.0	0.036	0.042	12.4	0.015	0.8	0.38
0.1	0.013	0.020	15.0	0.014	1.0	0.014	0.021	16.0	0.015	1.7	0.55
0.1	0.013	0.020	20.0	0.014	1.0	0.014	0.023	22.3	0.015	1.8	0.36

Note: Sun, 30° from zenith; wind speed, 5 m/s; observation angles (30°, 90°).

providing a measure of the fractional difference between the two curves.

C. Optimization

Optimization or minimization is effectively a predictor–corrector, model-inversion scheme, achieved by adjusting the values of the variables in the SA-model in response to the *err* function. For nonlinear optimization, initial values are important for the process. We set the values in the following manner, which has no relationship to ground truth values:

$$P^{\text{in}} = 0.072[R_{rs}{}^{\text{in}}(440)/R_{rs}{}^{\text{in}}(550)]^{-1.62} \text{ (Ref. 33)},$$

$$G^{\text{in}} = P^{\text{in}},$$

$$X^{\text{in}} = 30a_w(640)R_{rs}{}^{\text{in}}(640),$$

$$B^{\text{in}} = 0.2 \text{ [equivalent to } \rho(550) = 0.2\text{]},$$

$$H^{\text{in}} = 10.0,$$

$$\Delta^{\text{in}} = R_{rs}{}^{\text{raw}}(750).$$

For each set of values for the six unknowns an optimization program computes the *err* value of Eq. (24) and repeats the process with different sets of values until *err* reaches a minimum. At that point, values for P, G, X, B, and H are then considered to be derived. In the process, values for P, G, X, B, and H are kept positive. Note that no field data are required except the measured $R_{rs}{}^{\text{raw}}(\lambda)$ curves.

The performance of the above model-inversion scheme can be tested by using perfect Hydrolight-generated data for the first test and field data for the second.

4. Data

A. Computer-Simulated Data

Using a particle phase function typical of coastal waters,[34] we calculated above-surface upwelling radiance values observed at 30° to nadir and 90° to the solar plane and downwelling irradiance and sky radiance with Hydrolight 3.0.[18] Tables 2 and 3 provide information regarding the inputs used in the computer simulations. Wind speeds of 5 and 10 m/s were used with the Sun at 10°, 30°, and 60° from zenith. The water column was assumed to be homogeneous. The solar input and the bio-optical models used in the calculations are discussed in detail in Ref. 13 (see Appendix A). In the simulations the bio-optical parameter $\Re$ for particle scattering at 550 nm (see Ref. 13 or Appendix A) was set at 1.0 to indicate a possible higher sediment loading in coastal waters. A 20% cloud fraction was applied to the calculation. As in Ref. 13, a spectrally constant bottom albedo was applied for data simulation.

In total, T_{rs} for seven depths, two wind speeds, and three sun angles was calculated. It included chlorophyll-a concentrations ranging from 0.1 to 2.0 mg/m^3 and bottom depths ranging from 2.0 to 20.0 m. These calculations were intended to test the semianalytical model and the inversion process for different

Table 3. Input Values to Hydrolight Calculation Compared with Inversion-Derived Values

Input						Inversion					
[chl-a]	$a_\phi(440)$	$a_g(440)$	H	S	Y	$a_\phi(440)$	$a_g(440)$	H	S	Y	w
2.0	0.094	0.141	2.0	0.014	1.0	0.100	0.131	2.1	0.015	0.5	0.78
2.0	0.094	0.141	5.0	0.014	1.0	0.107	0.094	4.9	0.015	0.2	0.51
1.0	0.060	0.090	4.0	0.014	1.0	0.065	0.078	4.2	0.015	0.4	0.73
1.0	0.060	0.090	8.0	0.014	1.0	0.066	0.065	7.9	0.015	0.4	0.41
0.4	0.033	0.050	8.0	0.014	1.0	0.035	0.044	8.5	0.015	0.8	0.62
0.4	0.033	0.050	12.0	0.014	1.0	0.035	0.042	12.3	0.015	0.8	0.40
0.1	0.013	0.020	15.0	0.014	1.0	0.014	0.021	16.0	0.015	1.7	0.56
0.1	0.013	0.020	20.0	0.014	1.0	0.013	0.023	22.0	0.015	1.8	0.38

Note: Sun, 30° from zenith; wind speed, 10 m/s; observation angles (30°, 90°).

Table 4. Field Data

Location		*In Situ*				Inversion					
Latitude (North)	Longitude (West)	[chl-a]	$a_\phi(440)$	$a_g(440)$	H	$a_\phi(440)$	$a_g(440)$	H	Y	w	Err
25.127	80.809	2.32	0.070		0.8	0.068	0.530	1.3	0	0.49	0.01
25.08	80.757	0.98	0.051		1.6	0.037	0.333	2.0	0	0.53	0.01
25.065	80.67	1.43	0.055		1.8	0.021	0.181	2.6	0	0.32	0.01
25.034	80.589	0.58	0.028		1.7	0.005	0.158	2.1	1	0.23	0.02
24.985	80.434		0.021		8.0	0.012	0.032	7.9	0.9	0.75	0.02
24.975	80.494		0.016		5.5	0.005	0.124	5.1	0	0.70	0.03
24.955	80.477		0.014		5.5	0.014	0.029	5.3	1.2	0.70	0.02
24.534	81.465		0.038		6.5	0.027	0.108	5.5	0.3	0.36	0.02
24.55	81.414		0.020		8.0	0.017	0.050	8.2	0.9	0.42	0.02
24.714	81.169	0.31	0.022	0.240	3.5	0.033	0.209	3.7	0	0.46	0.02
24.624	81.119	0.42	0.025	0.031	7.6	0.015	0.026	8.4	1.1	0.73	0.02
24.624	81.12	0.36	0.025	0.025	8.2	0.016	0.030	8.0	0.8	0.79	0.03
24.625	81.105	0.32	0.025	0.023	10.9	0.015	0.030	9.3	1.5	0.51	0.02
24.69	81.12	0.51	0.036	0.210	3.5	0.028	0.160	3.4	0.1	0.33	0.02
27.342	83.054	0.43	0.043		16.0	0.027	0.078	13.4	0.5	0.42	0.02
27.592	83.039	0.61	0.031		25.0	0.026	0.032	23.9	1.5	0.16	0.02
27.602	82.995	0.66	0.043	0.059	17.5	0.013	0.046	18.3	0.7	0.32	0.03
27.594	82.925	0.42	0.025	0.063	14.5	0.013	0.061	15.3	0.4	0.30	0.02
27.605	82.812	0.8	0.040	0.100	8.4	0.034	0.098	8.3	0.3	0.24	0.01
27.564	82.762	1.40	0.077	0.203	8.5	0.005	0.260	7.1	0	0.53	0.03
27.374	82.746	0.21	0.046	0.132	11.9	0.032	0.094	10.6	0	0.63	0.02
24.678	81.908	0.46	0.021	0.056	10.7	0.011	0.053	11.3	0.5	0.41	0.02
23.78	76.10	0.12	0.011	0.034	16.8	0.006	0.028	16.0	0.7	0.78	0.01
23.785	76.101	0.12	0.010	0.033	18.0	0.007	0.022	17.3	1	0.76	0.02
23.778	76.09	0.16	0.014	0.027	15.9	0.012	0.031	16.1	0.7	0.64	0.02
23.77	76.08	0.15	0.012	0.033	16.8	0.009	0.024	17.0	0.9	0.72	0.02
23.78	76.11	0.13	0.012	0.038	22.0	0.012	0.030	17.6	0.7	0.56	0.02
23.779	76.119	0.20	0.016	0.055	7.6	0.013	0.054	7.2	0.2	0.85	0.02
23.78	76.119	0.13	0.015	0.049	8.0	0.006	0.053	7.8	0.1	0.87	0.01
23.79	76.107	0.10	0.012	0.025	13	0.007	0.037	15.9	0.4	0.65	0.02
25.2	82.06				20.7	0.018	0.061	18.2	0.8	0.32	0.02
25.207	82.069	0.24	0.024	0.106	22.0	0.018	0.079	20.9	0.8	0.23	0.02
25.712	82.224	0.31	0.038	0.187	20.4	0.029	0.133	18.5	0.3	0.23	0.03
26.428	82.448				19.2	0.021	0.054	22.3	0.6	0.32	0.02
23.786	76.101	0.13	0.011	0.030	16.2	0.005	0.032	15.5	0.3	0.91	0.03
23.78	76.09	0.07	0.012	0.035	16.5	0.008	0.026	16.2	0.9	0.73	0.02
23.77	76.1	0.16	0.013	0.033	15.9	0.012	0.031	17.1	0.7	0.58	0.02

situations, in which all derived values could be compared with exact input values for Hydrolight. Field comparisons are used as a more realistic evaluation of the method, at least for environments similar to Florida shelf waters.

B. Field Data

From 1990 to 1998 a series of field measurements were taken over shallow waters along the west Florida shelf, Key West, Fla., and the Bahamas. The water depths ranged from 0.8 to 25.0 m; [chl-a] ranged from 0.3 to 2.3 mg/m^3. In the left panel of Table 4 water-property information is summarized, whereas Fig. 3 presents most of the sites on a regional map. For each station, hyperspectral T_{rs}, S_{rs}, particle and pigment absorption coefficients (a_p and a_ϕ) and gelbstoff absorption for some of the surface-water samples were measured. Depth was determined acoustically ($\pm$0.3 m) for the deeper waters and with a lead-weighted line ($\pm$0.1 m) for Florida Bay stations. Only the T_{rs} and S_{rs} data were used as inputs to the inversion process. The other measurements were reserved to validate the method.

1. Total-Remote-Sensing Reflectance T_{rs} and Sky Input S_{rs}

Hyperspectral T_{rs} and S_{rs} were calculated by the method of Lee *et al.*[23] Briefly, using a Spectron Engineering spectroradiometer (Spectron Model SE-590, Spectrix for 1997 and later), a series (~3 to 5 scans) of upwelling radiance above the surface [$L_u(0^+, \theta_a, \varphi)$] and downwelling sky radiance [$L_{\text{sky}}(\theta', \varphi)$] was directly measured with θ_a (viewing angle in the air) $\approx$ 30° from nadir and φ approximately 90° from the solar plane. Sky radiance was measured in the same plane as $L_u(0^+)$ but from a direction of $\theta' \approx$ 30° from zenith. Downwelling irradiance was derived by measuring the radiance L_G reflected from a standard diffuse reflector (Spectralon). For each of

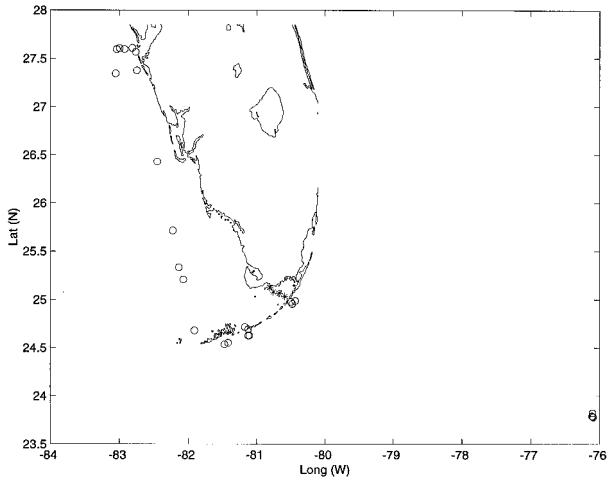

Fig. 3. Locations of field data.

the measured scans, T_{rs} and S_{rs} were derived through

$$T_{rs} = \frac{L_u}{L_G}\frac{R_G}{\pi}, \qquad S_{rs} = \frac{L_{\text{sky}}}{L_G}\frac{R_G}{\pi}, \tag{25}$$

where R_G is the reflectance of the diffuse reflector ($\sim$10%).

Based on these measured T_{rs} and S_{rs} curves, averages of T_{rs} and S_{rs} were obtained, respectively, to reduce the random variations associated with measurements owing to reflection from different wave facets etc. These averaged curves are used in the inversion process with an $F(30)$ value of 0.022 for deriving R_{rs}^{raw}.

2. Absorption Coefficient of Particles and Pigments, a_p and a_ϕ

The $a_\phi(\lambda)$ was measured following the SeaWiFS protocols.[35] Basically the method described in Ref. 36 was used to measure the particle absorption coefficient on the GF/F filter pad a_p, and the method developed by Kishino *et al.*[37] and modified by Roesler *et al.*[38] was used to measure the detritus absorption on the pad a_d to calculate the phytoplankton absorption coefficient a_ϕ. The β factor from Bricaud and Stramski[39] [their Eq. (2)] for the correction of the optical-path elongation due to filter-pad multiple scattering was used for the calculations of a_p and a_d. Large-particle scattering was removed when $a_p(780) = 0$ was assumed. The difference between the particle and the detrital absorption coefficients provided the absorption coefficient of phytoplankton pigments a_ϕ:

$$a_\phi = a_p - a_d. \tag{26}$$

3. Absorption Coefficient of Gelbstoff a_g

Samples for a_g were obtained by filtering seawater samples first through preflushed 47-mm GF/F filters and then through 47-mm, 0.2-μm polycarbonate filters. Absorption spectra were measured in 10-cm quartz cuvettes by use of a Perkin-Elmer Lambda 18 dual-beam spectrophotometer.

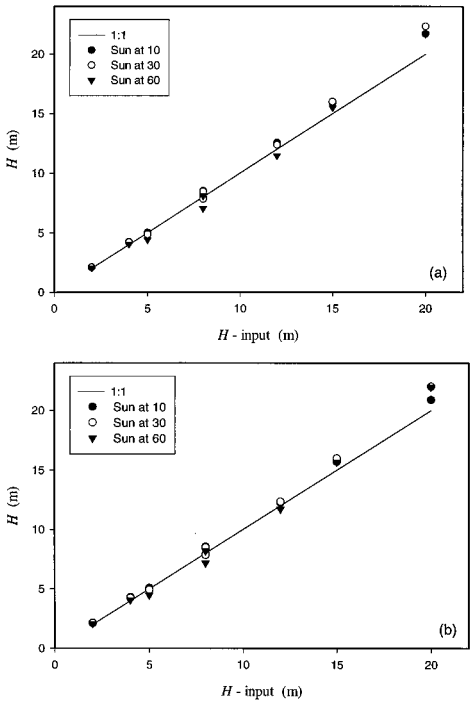

Fig. 4. (a) Inversion-derived depths compared with input values for simulated data with 5 m/s of wind. (b) As in (a) with 10 m/s of wind.

5. Results and Discussion

A. Computer-Simulated Data

For the computer-generated data a spectrally constant bottom-albedo shape was used in the inversion process. For the three sun angles the mean difference for depths was 5.3% between the SA-model inversions and Hydrolight data for 5-m/s wind speed and 5.1% for 10-m/s wind speed (see Fig. 4 and Tables 2 and 3). For comparison of two data sets the difference δ was calculated as in Ref. 23 to provide equal weighting to underestimation as well as overestimation:

$$\delta = \exp\left[\text{mean}\left|\ln\left(\frac{Q_i^{\text{der}}}{Q_i^{\text{mea}}}\right)\right|\right] - 1, \tag{27}$$

where Q_i represents the individual quantity such as the depth or the absorption coefficient. Q_i^{der} represents the derived value, whereas Q_i^{mea} represents either the Hydrolight input or the field-measured value.

As an example, for the Sun at a 30° zenith angle and wind speeds of 5 and 10 m/s, the derived bottom depths along with in-water optical properties are listed in the right panel of Tables 2 and 3, respectively, with input values to Hydrolight listed at the left side for comparison. For other sun angles, results are indicated in Figs. 5–15. In Tables 2–4 w is defined as

$$w = \max\left[\frac{r_{rs}^{B}(\lambda)}{r_{rs}(\lambda)}\right], \tag{28}$$

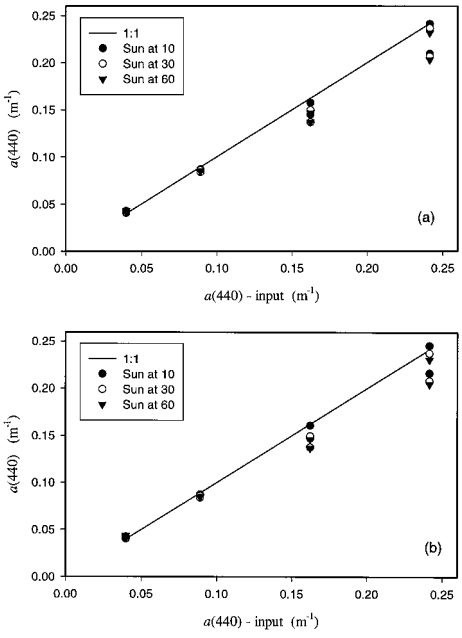

Fig. 5. (a) Inversion-derived total absorption at 440 nm compared with input values for simulated data with 5 m/s of wind. (b) As in (a) with 10 m/s of wind.

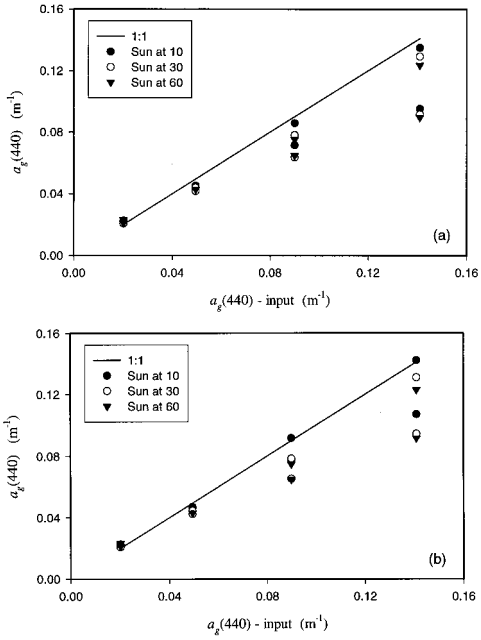

Fig. 7. (a) Inversion-derived gelbstoff absorption at 440 nm compared with input values for simulated data with 5 m/s of wind. (b) As in (a) with 10 m/s of wind.

or the maximum ratio of bottom contribution to the total for each case, calculated with inversion-derived data. In this study stations with w values of less than 0.15 were not included. R_{rs} at those stations was less sensitive to the depth, and reliable depth values were not expected. This criterion provides a useful operational constraint.

Generally the retrieved depths agreed with the Hydrolight input depths very closely (~5% difference) with slight overestimations for deeper depths (see Fig. 4), where the Y values used in the inversion were much larger than the Y values in computer simulations (see Tables 2 and 3).

In Fig. 5 we compare the derived $a(440)$ with the

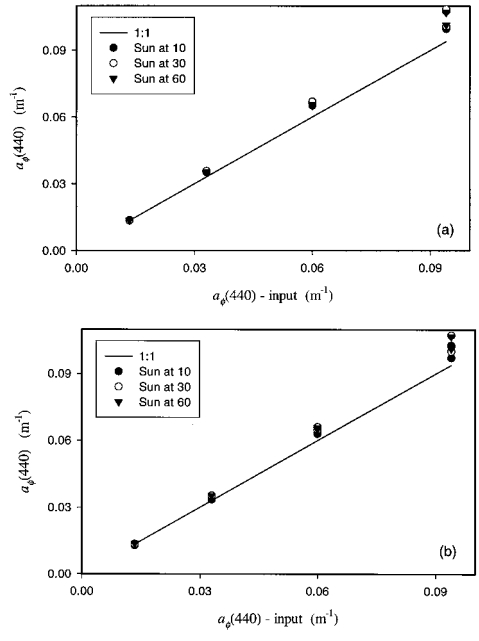

Fig. 6. (a) Inversion-derived pigment absorption at 440 nm compared with input values for simulated data with 5 m/s of wind. (b) As in (a) with 10 m/s of wind.

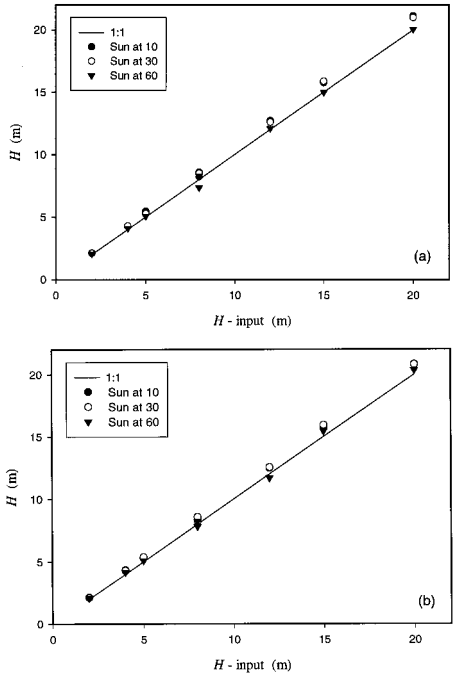

Fig. 8. (a) Inversion-derived depths compared with input values for simulated data with 5 m/s of wind. The Y value used in inversion was random (see text). (b) As in (a) with 10 m/s of wind.

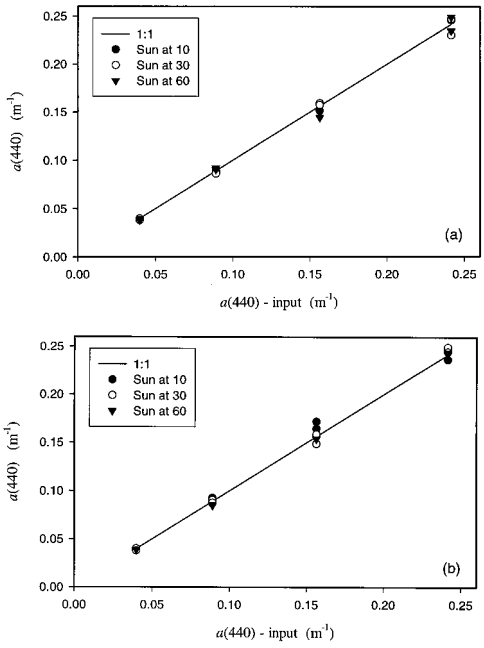

Fig. 9. (a) Inversion-derived total absorption at 440 nm compared with input values for simulated data with 5 m/s of wind. The Y value used in inversion was random (see text). (b) As in (a) with 10 m/s of wind.

known input values. For the three sun angles the average δ value was 7.0% for 5-m/s wind speed and 6.3% for 10-m/s wind speed for $a(440)$ values ranging from 0.04 to 0.24 m^{-1}. In Fig. 6 we compare the derived $a_\phi(440)$ with the known input values, with δ values of 7.1% and 6.0% for 5- and 10-m/s wind speeds, respectively. In Fig. 7 we compare the derived $a_g(440)$ with the known input values, with δ values of 18.6% and 16.2% for the two wind speeds.

From what we observe here the maximum difference occurred for the inversion of a_g, which then causes differences for other properties of interest. Reasons for this larger difference are the following: First, the spectral curvatures between $b_{bp}(\lambda)$ and $a_g(\lambda)$ are somewhat similar, which causes compensation between the values of G and X. Generally, smaller Y values will result in smaller $a_g(440)$ and larger Y values will result in larger $a_g(440)$ in the inversion. Second, the values of Y used in the inversion were based on an estimation from using Eq.

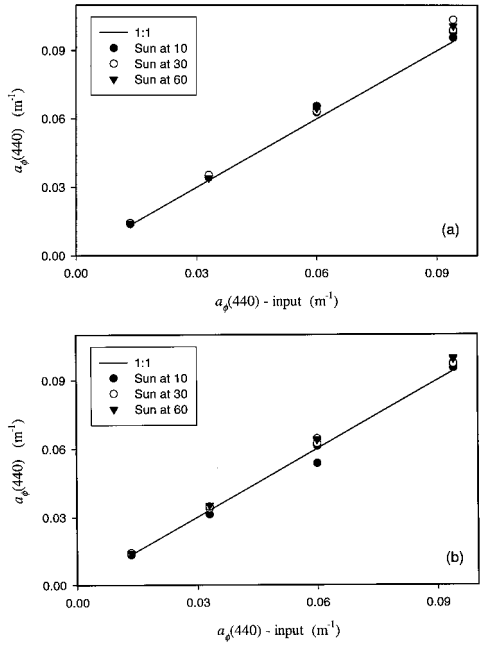

Fig. 10. (a) Inversion-derived pigment absorption at 440 nm compared with input values for simulated data with 5 m/s of wind. The Y value used in inversion was random (see text). (b) As in (a) with 10 m/s of wind.

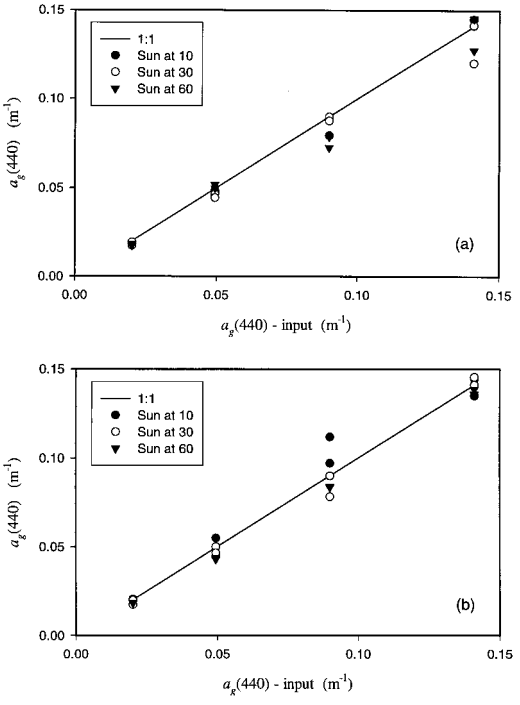

Fig. 11. (a) Inversion-derived gelbstoff absorption at 440 nm compared with input values for simulated data with 5 m/s of wind. The Y value used in inversion was random (see text). (b) As in (a) with 10 m/s of wind.

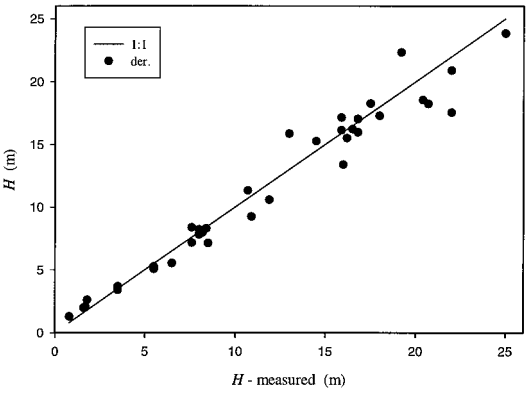

Fig. 12. Inversion-derived depths compared with field data.

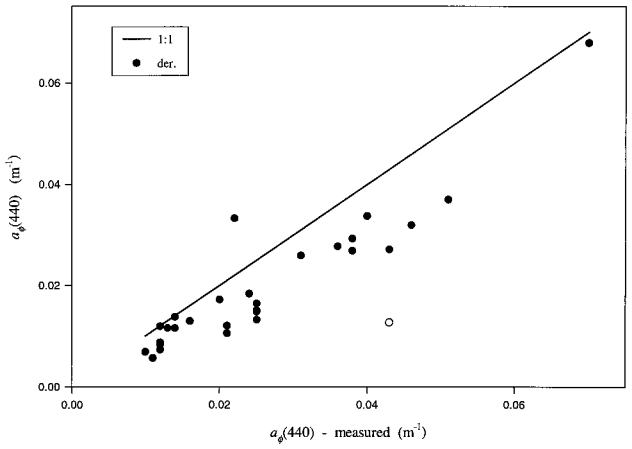

Fig. 13. Inversion-derived pigment absorption coefficient at 440 nm compared with pad-measured values for field data. (The open circle one was not used in error calculation.)

(20) instead of the known input values (see Tables 2 and 3), since theoretically a remote sensor does not know the actual Y value of the water. In the natural field Y values are generally lower for high concentrations of chlorophyll and higher for the open ocean with low chlorophyll.[40] For the inversion process estimations of Y were empirically based on the variation of the natural field,[14] but Hydrolight Y values were kept constant in the computer simulation no matter what the chlorophyll concentration was. The estimated Y then will not match the input Y value for each case (we see a factor of 5–10 difference for some cases), and we see a larger difference in the $a_g(440)$ estimation as a result.

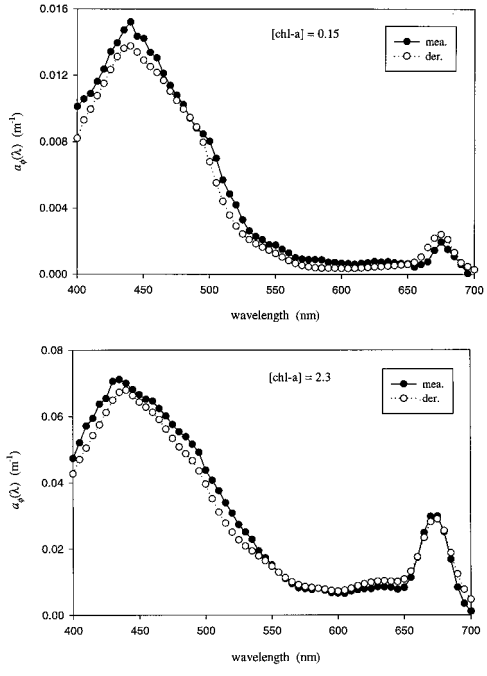

Fig. 14. Examples of inversion-derived versus pad-measured pigment absorption spectra.

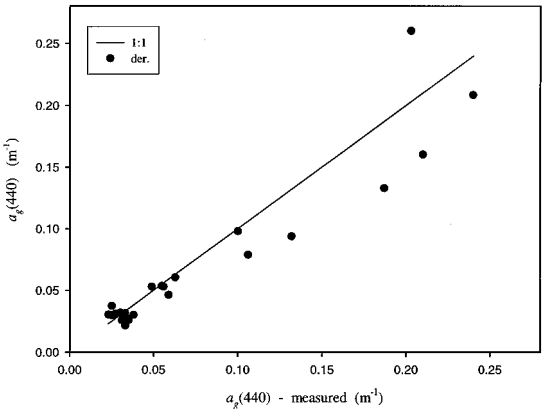

Fig. 15. Inversion-derived gelbstoff absorption coefficient at 440 nm compared with measured values for field data.

To see the inversion improvement if better estimated Y values were found, another round of inversion calculations was made by letting the Y value in the inversion be randomly determined between 0.6 and 1.4 for each case. In Fig. 8 we compare the H values for the three sun angles, in Fig. 9 the $a(440)$ values, in Fig. 10 the $a_\phi(440)$ values, and in Fig. 11 the $a_g(440)$ values. This time, for a 5-m/s wind speed the difference was 4.7% for H, 2.9% for $a(440)$, 5.6% for $a_\phi(440)$, and just 7.4% for $a_g(440)$; for a 10-m/s wind speed, the difference is 4.8% for H, 2.4% for $a(440)$, 4.6% for $a_\phi(440)$, and just 7.0% for $a_g(440)$. We see that the differences were greatly reduced especially for $a_g(440)$, and the accuracy for all properties of interest was improved. These results suggest the importance of good estimations of the Y value in the remote-sensing inversion.

The S values used in the inversion were not far from the input values. In a manner similar to the above discussion we can expect an influence of different S values on the inversion results. Contrary to the influence of Y values on the inversion, however, the value of S has a smaller influence on H, but more influence on P and G values, because the effect of $a_g(\lambda)$ is more important at the shorter wavelengths and the effect on H depends on the total absorption coefficient, not just on $a_g(\lambda)$.

B. Field Data

For the field data the mean difference for depth was 10.9% or 1.4 m of the rms error for a range of 0.8–25 m ($R^2 = 0.96, N = 37$, see Fig. 12). If we ignore the four stations (* in Fig. 3) in Florida Bay, the difference was just 8.1%. This kind of result suggests that the model and the optimization method work very well in retrieving the bottom depths. Larger depth differences were found for the Florida Bay stations, where water was very turbid (with b_b/a as high as 1.6) and the bottom structure was more complicated. Further studies are needed to diagnosis the discrepancies, but turbidity is probably the most important factor.

Of the field data, $a_\phi(440)$ had a range of 0.010–0.070 m^{-1} and $a_g(440)$ had a range of 0.023–0.24 m^{-1}

from water-sample measurements. These data indicate that the study sites contain a wide variation of optical properties of the water column and are certainly not case 1 waters.[21] For $a_\phi(440)$ where retrieved ratios of $a_\phi(440)/a_g(440) > 1/8$, the difference is 42.7% ($N = 28$) (see Fig. 13). When $a_\phi(440)/a_g(440) < 1/8$, remote-sensing reflectance in the blue-green region is less sensitive to the value of $a_\phi(440)$ and is dominated by the influence of a_g values.

Figure 14 shows examples of retrieved-versus-measured $a_\phi(\lambda)$ spectra for low and high chlorophyll concentrations, and we see a good match in the shapes. This match is important for calculating photons absorbed by phytoplankton pigments for photosynthesis.

The difference between inverted and pad-measured $a_\phi(440)$ values were large compared with the differences for depth and $a_g(440)$, owing in part to the quite small $a_\phi(440)/a_g(440)$ ratio (ranging from 0.13 to 0.8 with an average of 0.27) for these coastal waters, compared with normally approximately 1.3–2.5 for open ocean waters.[41] Some of the difference resulted from errors in the SA-model and the shape parameters (S and Y values, for example) used in the retrieval. Some of the differences, however, may come from the a_ϕ measurement itself. This is inferred since the derived H values are very comparable with the *in situ* values, and there is not much difference regarding $a_\phi(440)$ in the computer-simulated data sets where no measurement error is involved. Other possible causes may include the lack of any consideration of gelbstoff fluorescence in the model, which may be rather significant for such a gelbstoff-dominated environment.

The difference was 22.5% ($N = 24$) for $a_g(440)$ (see Fig. 15). As derived $a_g(440)$ is a combination of gelbstoff plus detritus; we would expect an overestimation in $a_g(440)$ values. However, we see that both $a_\phi(440)$ and $a_g(440)$ values were generally underestimated. To identify the error sources precisely regarding the difference in $a_\phi(440)$ and $a_g(440)$ values, we need a total absorption coefficient valued for the water column. Unfortunately we lack this measurement for the data sets evaluated.

The differences between retrieved and true values can come from many places. First, the SA-model was developed for normal coastal waters with an average particle phase function.[18] This SA-model may be inappropriate for extreme cases such as the Florida Bay waters. Second, there are errors in the SA-model, especially for viewing angles other than nadir. When we use the model to perform predictor–corrector inversions, those model errors will be transferred to the variables of the derivation. Third, because the spectral shape parameters such as S and Y cannot be accurately estimated from remote-sensing data, the errors associated with those parameters will be transferred to the properties of interest. Finally, field data contain measurement errors, and it is hard to ascertain knowledge of the homogeneity of water and bottom structures. Considering all these difficulties and uncertainties, a difference of 8–11% for depths suggests that the model and approach developed here work very well in retrieving shallow-water depth from remote sensing in these quite complicated coastal waters. More study is necessary to be able to say the same for the retrieval of water-column properties, however.

6. Summary

A model and an inversion method have been developed for the retrieval of bottom depth and in-water optical properties for a broad range of water types. The model and approach were applied to computer-simulated and field-measured data for shallow waters with a uniform, sand-type bottom. For computer-simulated data the retrieved depth was in general accurate to within 5% for a range of 2.0–20.0 m, and for field data it was accurate to within 11% ($N = 37$) for a range of 0.8–25 m. For data outside Florida Bay, however, it was within 8% ($N = 33$) for depth. Larger differences occurred in the retrieval of pigment absorption coefficients for the field data, but not for the computer-simulated data, which suggests that some of the measured pigment absorption values or their model simulations need further analysis. These results suggest that the model and approach developed here can be used for many coastal remote-sensing applications, but knowledge of the spectral shapes of phytoplankton and gelbstoff absorption and spectral shape of particle scattering would be helpful for better results in any given region.

As a result of these analyses, phase functions more consistent with the turbid waters of Florida Bay will be considered for new parameterization of the SA model. Clearly, higher backscattering efficiency is required for suspended mineral sediments than for the biogenous particles dominating the average particle phase function of Mobley.[34] The addition of gelbstoff fluorescence will also be considered in future retrievals in gelbstoff-rich waters.

Appendix A: Semianalytical Model for Remote-Sensing Reflectance of Shallow Waters

Based on quasi-single-scattering theory,[42] subsurface, nadir-viewing, remote-sensing reflectance is described as

$$r_{rs} = r_{rs}^{dp}\left(1 - \alpha_0 \exp\left\{-\left[\frac{1}{\cos(\theta_w)} + D_0(1 + D_1 u)^{0.5}\right]\kappa H\right\}\right) + \alpha_1 \rho \exp\left\{-\left[\frac{1}{\cos(\theta_w)} + D_0'(1 + D_1' u)^{0.5}\right]\kappa H\right\}, \tag{A1}$$

with

$$r_{rs}^{dp} = (g_0 + g_1 u^{g2})u \tag{A2}$$

for optically deep waters where $u \equiv b_b/(a + b_b)$, $\kappa \equiv a + b_b$. The terms $g_0, g_1, g_2, \alpha_0, \alpha_1, D_0, D_1, D_0'$, and D_1' are model parameters and are spectrally constant. To use Eqs. (A1) and (A2) to model r_{rs} when a, b_b, ρ, and H are known, values of the model parameters need to be determined. Lee *et al.*[13] derived those values by fitting Eqs. (A1) and (A2) to a large

set of r_{rs} values that were created by using a precise numerical model, Hydrolight.[18]

In the numerical simulation, wind speed was set at 5 m/s, the water body was assumed homogeneous, and solar zenith angles were set at 0°, 30°, and 60°. An average particle phase function described in Mobley *et al.*[34] was used. The scattering of pure seawater was treated as a separate component with a Rayleigh-like phase function.[34] Chlorophyll concentration was used as a surrogate to determine the coefficients of particle absorption and scattering, by use of simple bio-optical models.

The total absorption coefficient is expressed as a sum of the absorption coefficients for pure water, phytoplankton pigments, and gelbstoff. Absorption values for pure water were taken from Ref. 26, whereas absorption for phytoplankton pigments and gelbstoff were modeled as follows:

$$a_\phi(440) = 0.06\,[\text{chl-}a]^{0.65},[43] \tag{A3}$$

$$a_g(\lambda) = a_g(440)\exp[-0.014(\lambda - 440)],[28] \tag{A4}$$

and $a_\phi(\lambda)$ was simulated with the model of Lee *et al.*[13]

The total scattering coefficient is expressed as a sum of the scattering coefficients for pure seawater and particles. Scattering coefficients for pure seawater come from Morel,[31] whereas scattering coefficients for particles come from the model of Gordon and Morel,[43]

$$b_p(\lambda) = (550/\lambda)\Re[\text{chl-}a]^{0.62}. \tag{A5}$$

Here $\Re$ is a bio-optical parameter, which was 0.3 in Gordon and Morel.[43] $\Re$ values of 0.3, 1.0, and 5.0 were used to simulate a range from normal to highly turbid coastal waters.

A spectrally constant bottom albedo ρ was used with values of 0, 0.1, 0.3, and 1.0. Although the bottom reflectance was taken to be independent of wavelength, the inherent optical properties of the water column were wavelength dependent. This dependence allowed the fractional contribution of bottom-to-total radiance to be wavelength dependent.

By fitting Hydrolight-simulated r_{rs} for both deep and shallow situations, Lee *et al.*[13] derived the model-parameter values that follow:

$$g_0 \approx 0.07, \quad g_1 \approx 0.155, \quad g_2 \approx 0.752;$$
$$\alpha_0 \approx 1.03, \quad \alpha_1 \approx 0.31;$$
$$D_0 \approx 1.2, \quad D_1 \approx 2.0;$$
$$D_0' \approx 1.1, \quad D_1' \approx 4.9.$$

Recently, with more Hydrolight-simulated data, and correcting a calculation error in the earlier study, the above values were updated as

$$g_0 \approx 0.084, \quad g_1 \approx 0.170, \quad g_2 = 1;$$
$$\alpha_0 = 1, \quad \alpha_1 = 1/\pi;$$
$$D_0 \approx 1.03, \quad D_1 \approx 2.4;$$
$$D_0' \approx 1.04, \quad D_1' \approx 5.4.$$

Therefore the SA model for subsurface remote-sensing reflectance is

$$r_{rs} \approx r_{rs}^{dp}\left(1 - \exp\left\{-\left[\frac{1}{\cos(\theta_w)} + 1.03(1 + 2.4u)^{0.5}\right]\kappa H\right\}\right) + \frac{1}{\pi}\rho\exp\left\{-\left[\frac{1}{\cos(\theta_w)} + 1.04(1 + 5.4u)^{0.5}\right]\kappa H\right\}, \tag{A6}$$

with

$$r_{rs}^{dp} \approx (0.084 + 0.17u)u. \tag{A7}$$

Since satellite sensors measure radiance above the surface, the relationship between R_{rs} and r_{rs} must be known. There is[13,43,44]

$$R_{rs} = \frac{\zeta r_{rs}}{1 - \Gamma r_{rs}}, \tag{A8}$$

Eq. (A8) is exact, where ζ and Γ are model parameters, and their values depend on viewing angle and water properties. The denominator $(1 - \Gamma r_{rs})$ accounts for the effects of internal reflection from water to air. Although this internal-reflection term is often ignored, especially for open-ocean waters, we retain it here because r_{rs} can be quite large for turbid or shallow waters. For remote-sensing applications the values of ζ and Γ in Eq. (A8) need to be determined. By comparison of the Hydrolight-generated R_{rs} and r_{rs} values, it was found that $\zeta \approx 0.5$ and $\Gamma \approx 1.5$ for remote-sensing observation angles.[17] Thus Eq. (A8) takes the specific form as used in this paper:

$$R_{rs} \approx \frac{0.5 r_{rs}}{1 - 1.5 r_{rs}}. \tag{A9}$$

Financial support was provided by NASA through grants NAG5-3446, NAS5-97137, NAS5-31716, the Office of Naval Research (ONR) through grant N00014-96-I-5013, and the National Oceanic and Atmospheric Administration (NOAA) Coastal Ocean Program R/NCOP-5. The development of Hydrolight was supported in part by the ONR Environmental Optics Program under various contracts to C. D. Mobley, who was supported for this study through contract N00014-97-C-0024. We are also grateful for helpful comments and suggestions by two anonymous reviewers.

References

1. F. C. Polcyn, W. L. Brown, and I. J. Sattinger, "The measurement of water depth by remote-sensing techniques," Rep. 8973-26-F (Willow Run Laboratories, University of Michigan, Ann Arbor, Mich., 1970).
2. D. R. Lyzenga, "Passive remote-sensing techniques for mapping water depth and bottom features," Appl. Opt. **17,** 379–383 (1978).
3. D. R. Lyzenga, "Remote sensing of bottom reflectance and water attenuation parameters in shallow water using aircraft and Landsat data," Int. J. Remote Sensing **2,** 71–82 (1981).
4. J. M. Paredes and R. E. Spero, "Water depth mapping from

passive remote-sensing data under a generalized ratio assumption," Appl. Opt. **22,** 1134–1135 (1983).
5. R. K. Clark, T. H. Fay, and C. L. Walker, "Bathymetry calculations with Landsat 4 TM imagery under a generalized ratio assumption," Appl. Opt. **26,** 4036–4038 (1987).
6. D. Spitzer and R. W. J. Dirks, "Bottom influence on the reflectance of the sea," Int. J. Remote Sensing **8,** 279–290 (1987).
7. N. T. O'Neill and J. R. Miller, "On calibration of passive optical bathymetry through depth soundings analysis and treatment of errors resulting from the spatial variation of environmental parameters," Int. J. Remote Sensing **10,** 1481–1501 (1989).
8. W. D. Philpot, "Bathymetric mapping with passive multispectral imagery," Appl. Opt. **28,** 1569–1578 (1989).
9. D. R. Lyzenga, "Shallow-water bathymetry using combined lidar and passive multispectral scanner data," Int. J. Remote Sensing **6,** 115–125 (1985).
10. W. D. Philpot, "Radiative transfer in stratified waters: a single-scattering approximation for irradiance," Appl. Opt. **26,** 4123–4132 (1987).
11. Z. P. Lee, K. L. Carder, S. K. Hawes, R. G. Steward, T. G. Peacock, and C. O. Davis, "A model for interpretation of hyperspectral remote-sensing reflectance," Appl. Opt. **33,** 5721–5732 (1994).
12. S. Maritorena, A. Morel, and B. Gentili, "Diffuse reflectance of oceanic shallow waters: influence of water depth and bottom albedo," Limnol. Oceanogr. **39,** 1689–1703 (1994).
13. Z. P. Lee, K. L. Carder, C. D. Mobley, R. G. Steward, and J. S. Patch, "Hyperspectral remote sensing for shallow waters: 1. A semianalytical model," Appl. Opt. **37,** 6329–6338 (1998).
14. K. L. Carder, F. R. Chen, Z. P. Lee, and S. Hawes, "Semianalytic MODIS algorithms for chlorophyll-*a* and absorption with bio-optical domains based on nitrate-depletion temperatures," J. Geophys. Res. **104,** 5403–5421 (1999).
15. R. W. Preisendorfer, *Hydrologic Optics Vol. 1: Introduction*, NTIS PB-259 793/8ST (National Technical Information Service, Springfield, Va., 1976).
16. B. R. Marshall and R. C. Smith, "Raman scattering and in-water ocean properties," Appl. Opt. **29,** 71–84 (1990).
17. A. Morel and B. Gentili, "Diffuse reflectance of oceanic waters (Part 2): Bidirectional aspects," Appl. Opt. **32,** 6864–6879 (1993).
18. C. D. Mobley, *Hydrolight 3.0 Users' Guide*, Final Report, SRI (SRI International, Menlo Park, Calif. 94025, 1995), Project 5632.
19. H. R. Gordon, R. C. Smith, and J. R. V. Zaneveld, "Introduction to ocean optics," in *Ocean Optics VI*, S. Q. Duntley, ed., Proc. SPIE **208,** 1–43 (1979).
20. K. L. Carder, S. K. Hawes, K. A. Baker, R. C. Smith, R. G. Steward, and B. G. Mitchell, "Reflectance model for quantifying chlorophyll-*a* in the presence of productivity degradation products," J. Geophys. Res. **96,** 20,599–20,611 (1991).
21. A. Morel and L. Prieur, "Analysis of variations in ocean color," Limnol. Oceanogr. **22,** 709–722 (1977).
22. W. W. Gregg and K. L. Carder, "A simple spectral solar irradiance model for cloudless maritime atmospheres," Limnol. Oceanogr. **35,** 1657–1675 (1990).
23. Z. P. Lee, K. L. Carder, T. G. Peacock, C. O. Davis, and J. L. Mueller, "Method to derive ocean absorption coefficients from remote-sensing reflectance," Appl. Opt. **35,** 453–462 (1996).
24. K. L. Carder and R. G. Steward, "A remote-sensing reflectance model of a red tide dinoflagellate off West Florida," Limnol. Oceanogr. **30,** 286–298 (1985).
25. R. W. Austin, "Inherent spectral radiance signatures of the ocean surface," in *Ocean Color Analysis* (Final Technical Report), S. Q. Duntley, ed., SIO Ref. 74-10 (Scripps Institution of Oceanography, La Jolla, Calif., 1974), pp. 2.1–2.20.
26. R. Pope and E. Fry, "Absorption spectrum (380–700 nm) of pure waters: II. Integrating cavity measurements," Appl. Opt. **36,** 8710–8723 (1997).
27. Z. P. Lee, "Visible-infrared remote-sensing model and applications for ocean waters," Ph.D. dissertation (University of South Florida, Department of Marine Science, St. Petersburg, Fla., 1994).
28. A. Bricaud, A. Morel, and L. Prieur, "Absorption by dissolved organic matter of the sea (yellow substance) in the UV and visible domains," Limnol. Oceanogr. **26,** 43–53 (1981).
29. C. S. Roesler and M. J. Perry, "*In situ* phytoplankton absorption, fluorescence emission, and particulate backscattering spectra determined from reflectance," J. Geophys. Res. **100,** 13,279–13,294 (1995).
30. K. L. Carder, R. F. Steward, R. R. Harey, and P. B. Ortner, "Marine humic and fulvic acids: their effects on remote sensing of ocean chlorophyll," Limnol. Oceanogr. **34,** 68–81 (1989).
31. A. Morel, "Optical properties of pure water and pure sea water," in *Optical Aspects of Oceanography*, N. G. Jerlov and E. S. Nielsen, eds. (Academic, New York, 1974), pp. 1–24.
32. Z. P. Lee, K. L. Carder, J. Marra, R. G. Steward, and M. J. Perry, "Estimating primary production at depth from remote sensing," Appl. Opt. **35,** 463–474 (1996).
33. Z. P. Lee, K. L. Carder, R. G. Steward, T. G. Peacock, C. O. Davis, and J. L. Mueller, "Remote-sensing reflectance and inherent optical properties of oceanic waters derived from above-water measurements," in *Ocean Optics XIII*, S. J. Ackleson, ed., Proc. SPIE **2963,** 160–166 (1996).
34. C. D. Mobley, *Light and Water: Radiative Transfer in Natural Waters* (Academic, New York, 1994).
35. J. L. Mueller and R. W. Austin, "Ocean optics protocols for SeaWiFS validation," NASA Tech. Memo. 104566, Vol. 5, S. B. Hooker and E. R. Firestone, eds. (NASA Goddard Space Flight Center, Greenbelt, Md., 1992).
36. B. G. Mitchell and D. A. Kiefer, "Chl-*a* specific absorption and fluorescence excitation spectra for light limited phytoplankton," Deep-Sea Res. **35,** 635–663 (1988).
37. M. Kishino, M. Takahashi, N. Okami, and S. Ichimura, "Estimation of the spectral absorption coefficients of phytoplankton in a thermally stratified sea," Bull. Mar. Sci. **37,** 634–642 (1985).
38. C. S. Roesler, M. J. Perry, and K. L. Carder, "Modeling *in situ* phytoplankton absorption from total absorption spectra in productive inland marine waters," Limnol. Oceanogr. **34,** 1510–1523 (1989).
39. A. Bricaud and D. Stramski, "Spectral absorption coefficients of living phytoplankton and nonalgal biogenous matter: a comparison between the Peru upwelling area and the Sargasso Sea," Limnol. Oceanogr. **35,** 562–582 (1990).
40. S. Sathyendranath, L. Prieur, and A. Morel, "A three-component model of ocean color and its application to remote sensing of phytoplankton pigments in coastal waters," Int. J. Remote Sensing **10,** 1373–1394 (1989).
41. J. J. Walsh, K. L. Carder, and F. E. Mueller-Karger, "Meridional fluxes of dissolved organic matter in the North Atlantic Ocean," J. Geophys. Res. **97,** 15,625–15,637 (1992).
42. H. R. Gordon, O. B. Brown, and M. M. Jacobs, "Computed relationship between the inherent and apparent optical properties of a flat homogeneous ocean," Appl. Opt. **14,** 417–427 (1975).
43. H. R. Gordon and A. Morel, *Remote Assessment of Ocean Color for Interpretation of Satellite Visible Imagery: A Review* (Springer-Verlag, New York, 1983), p. 44.
44. H. R. Gordon, O. B. Brown, R. H. Evans, J. W. Brown, R. C. Smith, K. S. Baker, and D. K. Clark, "A semianalytic radiance model of ocean color," J. Geophys. Res. **93,** 10,909–10,924 (1988).